Modelling cohesive laws in finite element simulations via an adapted contact procedure in ABAQUS

Feih, S.

Publication date:
2004

Document Version
Publisher's PDF, also known as Version of record

Risø–R–1463(EN)

Modelling cohesive laws in finite element simulations via an adapted contact procedure in ABAQUS

Stefanie Feih
Materials Research Department
Risø National Laboratory, Denmark

Risø National Laboratory, Roskilde, Denmark
July 2004

Abstract The influence of different fibre sizings on the strength and fracture toughness of composites was studied by investigating the characteristics of fibre cross-over bridging in DCB specimens loaded with pure bending moments. These tests result in bridging laws, which are obtained by simultaneous measurements of the crack growth resistance and the end opening of the notch. The advantage of this method is that these bridging laws represent material laws independent of the specimen geometry. However, the adaption of the experimentally determined shape to a numerically valid model shape is not straight-forward, and most existing publications consider theoretical and therefore simpler softening shapes. Two possible methods of bridging law approximation are explained and compared in this report. The bridging laws were implemented in a numerical user subroutine in the finite element code ABAQUS. The main emphasis of this report is based on the numerical aspects of the different approaches, i.e. implementation, mesh sensitivity and numerical convergence.

ISBN 87–550–3321–0(Internet)
ISSN 0106–2840

Print: Pitney Bowes Management Services Denmark A/S · 2004

Contents

1 Introduction

For glass fibre composites, the interfacial properties are controlled by the sizing, which is applied to the glass fibres during manufacture. For the same matrix system, a change of sizing results in changes of these properties, thereby influencing the mechanical properties such as strength and fracture toughness. The concept of strength is used for characterising crack initiation in composite design, while fracture toughness determines crack growth and damage development. In mode I crack growth in unidirectional fiber composites, fibre cross-over bridging occurs during cracking along the fiber direction. This failure mode plays an important role during delamination of fibre composites and splitting cracks around holes and notches. The fibre bridging zone must be modelled as a discrete mechanism on its own; failure is not just controlled by the cracking at the crack tip. The failure process can be described by a bridging law, which defines the relationship between the crack opening displacement and the local bridging tractions resulting from the bridging ligaments. Cohesive laws were measured experimentally in previous work. This report explains a possible and simple way of incorporating these laws into the commercial finite element code ABAQUS. Two methods of adapting the experimentally determined bridging laws for the numerical model are studied. Crack aspects, such as crack opening shape and the influence of bridging law parameters, are studied in detail based on the numerical results.

2 Bridging law measurement

The approach for the measurements of bridging laws is based on the application of the path independent J integral [1], and has been used recently to determine the bridging characteristics of unidirectional carbon fibre/ epoxy composites [2] and glass fibre composites [3]. A symmetric DCB specimen is loaded with pure bending moments M (Figure 1). This specimen is one of the few practical specimen geometries, for which the global J integral (i.e. the integral evaluated around the external boundaries of the specimen) can be determined analytically [1]:

$$J = 12(1 - \nu_{13}\nu_{31})\frac{M^2}{b^2 H^3 E_{11}} \tag{1}$$

E_{11} is the Young's modulus referring to the material directions, ν_{13} and ν_{31} are the major and minor Poisson's ratio, b is the width and H the beam height.

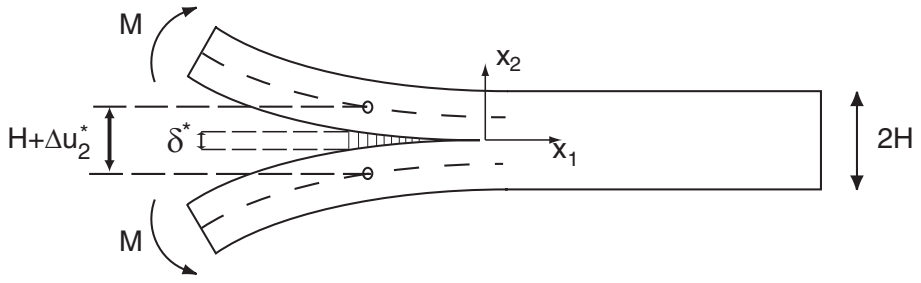

Figure 1. DCB specimen with pure bending moment

Now consider the specimen having a crack with bridging fibres across the crack faces near the tip. The closure stress σ (x_2-direction) can be assumed to depend only on the

local crack opening δ, i.e. the crack grows in pure mode I. The bridging law $\sigma = \sigma(\delta)$ is then taken as identical at each point along the bridging zone. Since fibres will fail when loaded sufficiently, we assume the existence of a characteristic crack opening δ_0, beyond which the closure traction vanishes. Shrinking the path of the J integral to the crack faces and around the crack tip [4] gives

$$J = \int_0^{\delta^*} \sigma(\delta) d\delta + J_{\text{tip}}, \tag{2}$$

where J_{tip} is the J integral evaluated around the crack tip (during cracking J_{tip} is equal to the fracture energy of the tip, J_0). The integral is the energy dissipation in the bridging zone and δ^* is the end-opening of the bridging zone at the notch root. The bridging law can be determined by differentiating equation 2 [4].

$$\sigma(\delta^*) = \frac{\partial J}{\partial \delta} \tag{3}$$

J_R and the end opening of the bridging zone Δu_2^* are recorded. Assuming that $\delta^* \approx \Delta u_2^*$, the bridging law can be determined. This approach models the bridging zone as a discrete mechanism on its own. Contrary to crack growth resistance curves (R-curves), the bridging law can be considered a material property and does not depend on specimen size [2].

3 Experimental results

Recently, we have, by the use of a J integral based approach, measured the bridging laws under mode I fracture during transverse splitting of unidirectional glass-fiber/epoxy and glass-fiber/ polyester composites with different interface characteristics [3]. With increasing applied moment, crack propagation took place. Fibre cross-over bridging developed in the zone between the notch and the crack tip.

J_R is calculated according to Eq. (1). The specimen width b was 5 mm with a beam height of H=8 mm. Assuming that the unidirectional composite is transversely isotropic, the following elastic composite data were applied for Eq. (1) as previously measured: $E_{11,\text{epoxy}}$= 41.5 GPa, E_{33}= 9.2 GPa, $E_{11,\text{polyester}}$ = 42 GPa, $E_{33,\text{polyester}}$= 10 GPa and ν_{13}=0.3 (assumption). The function

$$J_R(\delta^*) = J_0 + \Delta J_{\text{ss}} \left(\frac{\delta^*}{\delta_0} \right)^{\frac{1}{2}} \tag{4}$$

was found to fit all experimental data curves well, resulting in curve fits as shown in Figure 2(a). J_0 is the initial value of the experimental curve and equal to the fracture energy of the tip during crack growth, while ΔJ_{ss}, which is equal to $(J_{\text{ss}} - J_0)$, is the increase in crack growth resistance. Sørensen and Jacobsen [2] found that the same function fit the data of carbon fibre composite systems well.

The experimental values for the bridging laws are given in Table 1. The starting value

Table 1. Experimental values for the bridging law for different composite systems

Composite system	J_0 [J/m^2]	ΔJ_{ss} [J/m^2]	δ_0 [mm]
sizing A/epoxy	300 ± 40	4000 ± 1000	2.0 ± 0.2
sizing B/epoxy	355 ± 15	3700 ± 500	2.0 ± 0.2
sizing A/polyester	170 ± 20	3800	5.5
sizing B/polyester	115 ± 45	> 4100	> 5.0

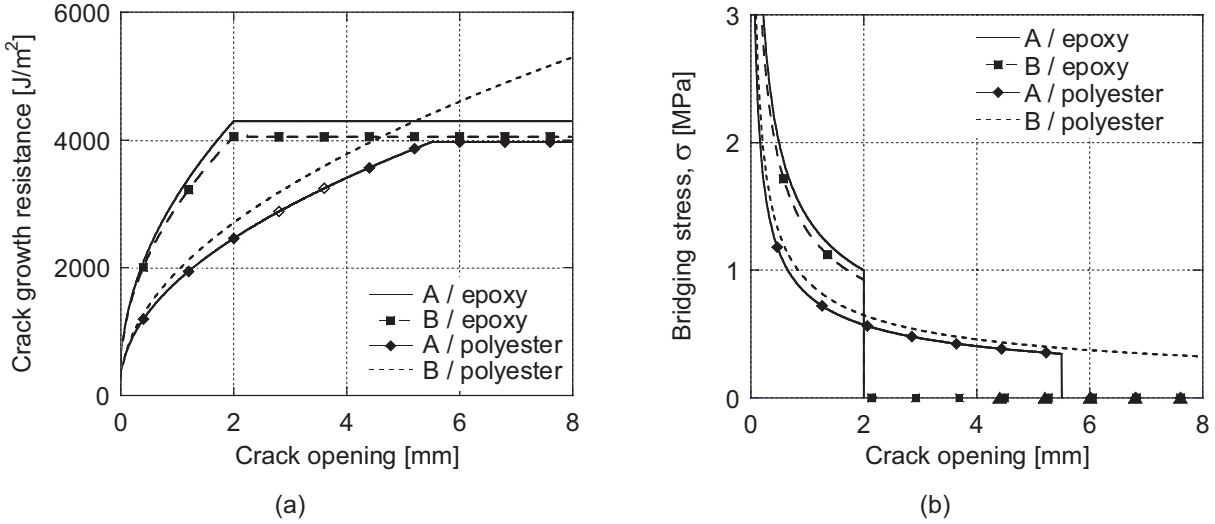

Figure 2. Comparison of (a) crack growth resistance and (b) resulting bridging laws

J_0 indicates the point of crack growth initiation and can easily be determined during the experiment. The highest value of 355 J/m^2 was observed for the sizing B/ epoxy system. The crack initiation value is significantly lower for the sizing B/ polyester system with 115 J/m^2, which is also related to a significantly lower transverse strength of not more than half the strength of the other composites [3].

The end opening value δ_0 at the onset of steady-state cracking was determined to be 2 mm for the epoxy systems. For the sizing B/ polyester system, steady-state cracking could not be determined with the present specimens, as the fibres continued to bridge the whole length of the crack after the maximum measurable notch opening of 5 mm was obtained. Since no upper bound was found for ΔJ_{ss}, this bridging behaviour was termed 'infinite toughening'.

Differentiating equation (4) results in the bridging law

$$\sigma(\delta) = \frac{\Delta J_{\text{ss}}}{2\delta_0}\left(\frac{\delta}{\delta_0}\right)^{-\frac{1}{2}}, \quad \text{for} \quad 0 < \delta < \delta_0, \tag{5}$$

where ΔJ_{ss} is the increase in crack growth resistance due to bridging (from zero to steady state bridging), and δ_0 is the crack opening where the bridging stress vanishes.

The bridging laws for the different fibre systems are compared in Figure 2(b). The bridging law can be considered a material property [2, 5] and is in an accessible form for implementation in finite element codes.

4 ABAQUS modelling procedure

There are a couple of possible methods for implementing cohesive laws within commercial finite element programs. The most versatile is most likely the development and programming of cohesive elements [6–8], which in most cases are defined with zero thickness and prescribe stresses based on the relative displacement of the nodes of the element. Similar work has also been undertaken with spring elements, although in this case there might be simplifications required when calculating the equivalent nodal spring forces from the stresses in the cohesive law. The procedure is not straight forward when springs are connected to elements with non-linear shape functions, such as 8-noded elements [9]. A relatively simple method is explained in the following: ABAQUS' internal

contact routine is adapted to account for the bridging stresses. This current work then focusses on the chosen bridging law shape and the resulting numerical issues, such as convergence problems, increment size, and modification of ABAQUS' solution parameters to enhance the program's performance for the specific task. The results will be used in future work to verify the programming of a cohesive element programmed in user subroutine UEL.

The beam-contact problem is shown in Figure 3. Owing to symmetry, it is sufficient to consider only one beam of the DCB specimen, although full models were run to check the contact approach. The thickness H is equal to 8 mm, as discussed in Section 3. Plane strain conditions were assumed, which neglect edge effects. The mesh consisted of eight-noded plane strain solid CPE8 elements, which are suited to describe bending deformations without hourglass effects. The composite material is assumed to be transversely isotropic. The material properties were given in the previous section.

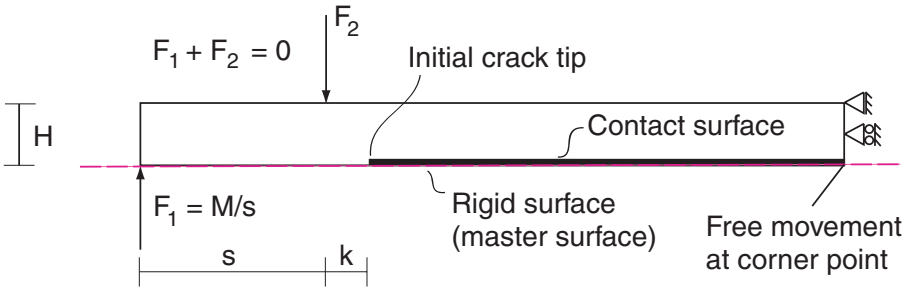

Figure 3. Problem statement and boundary conditions for pure moment loaded DCB specimen (symmetric half model)

In ABAQUS, most contact problems are modelled by using surface-based contact. For the case of the full DCB model, contact exists between two deformable bodies. For the symmetry case, on the other hand, contact between a rigid surface and a deformable body is considered (see Figure 3). In both cases the structures can be either two- or threedimensional.

There are three steps in defining a contact simulation: (1) Defining the surfaces of the bodies that could potentially be in contact, (2) specifying which surfaces interact with one another and (3) defining the mechanical surface interaction model that governs the behaviour of the surfaces when they are in contact.

For the third point, ABAQUS offers several mechanical surface interaction models. These include friction (interaction tangential to the surface), finite sliding (relative surface motions), softened contact (interaction normal to the surface) and user-defined constitutive modelling of the surface interaction. The latter is the most versatile option, and can be used to program the parameters of the cohesive law. For the general implementation of the cohesive law under mode I fracture, as explained in the previous section, only interaction normal to the fracture surface is considered. Friction and sliding can therefore be excluded. These options could possibly be adapted for mixed mode fracture.

4.1 Application of pure moment bending by displacement control

In analyses with possible decreasing stresses due to introduced material damage or decreasing bridging stresses, displacement controlled deformation, rather than force controlled, becomes the preferred way of introducing boundary conditions. Furthermore, displacement control is mostly applied in experimental testing and also in the case of the DCB specimen testing: testing procedure and simulation are therefore more closely

related.

The application of a homogeneous bending moment by force control requires consideration of the element type, where varying forces need to be applied to each node according to the underlying shape functions of the element type. This procedure does unfortunately not work for displacements, as for a given translation the rotation of the beam is unknown. The displacement controlled procedure introduced in the following was first described in previous work of the group [9]. The moment application is simplified, thereby resulting in a non-homogeneous displacement field towards the nodes of the applied boundary conditions at the end of the beam. However, pure bending conditions are introduced around the contact zone by ensuring that the distance k between moment introduction and beginning of the contact zone (see Figure 3) is large enough. The value is set to k=12 mm in the present model, with s being equal to 24.65 mm. As a rule of thumb, boundary conditions should be applied more than the beam thickness away from the point of interest to ensure a uniform bending stress in this region. With a beam height of H=8 mm, this requirement is fulfilled.

The displacements v_1 and v_2 of two nodes are to be controlled such that the resulting forces in the two nodes, F_1 and F_2, are equal and opposite in magnitude, thereby introducing a pure bending moment (see Figure 4). To accomplish this, v_1 and v_2 are

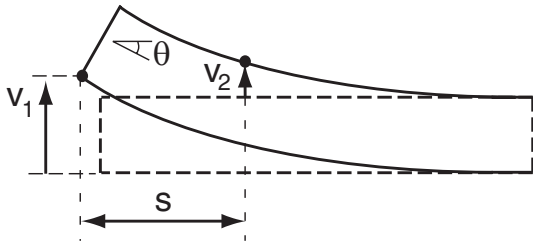

Figure 4. Displacements used for controlling the rotation and applying a pure moment to the beam arm of a DCB specimen

inter-connected by two so-called dummy nodes A and B, having displacement v_A and v_B, respectively. Dummy nodes are nodes that are not associated with the geometry. Their positions with respect to the beam structure are arbitrary, but their displacements have to be coupled to the structural deformation. In the following we derive a suitable relationship between v_1, v_2, v_A and v_B. The displacement of node A is defined as

$$v_A = v_1 - v_2. \tag{6}$$

Note that $\theta = \arctan(v_A/s) \approx v_A/s$ is the rotation of the beam, with s being the current difference in x-coordinates between nodes 1 and 2, i.e. the moment arm. The distance between the nodes will change during the analysis, which needs to be taken into account. The displacement in node B is set to

$$v_B = v_1 + v_2. \tag{7}$$

These definitions are mostly arbitrary. In a physical sense, they can be described as a rotational component (displacement ν_A) and a translational component (displacement ν_B). We have to make sure that the same energy is applied to the dummy nodes as is applied to the structure itself. Using the principle of virtual work, the applied incremental elastic energy dw is given by

$$dw = F_1 dv_1 + F_2 dv_2. \tag{8}$$

Similarly, the incremental elastic energy applied to nodes A and B is

$$dw = F_A dv_A + F_B dv_B, \tag{9}$$

where F_A and F_B are the forces in nodes A and B. Finally, the pure bending condition

$$F_1 + F_2 = 0 \tag{10}$$

must hold true. As the forces in the dummy nodes must (according to the principle of virtual work) perform the same incremental work as F_1 and F_2, the following relations are obtained:

$$\begin{aligned} dw &= F_A d(v_1 - v_2) + F_B d(v_1 + v_2) && (11)\\ &= (F_A + F_B)dv_1 + (F_B - F_A)dv_2 && (12) \end{aligned}$$

In comparison with Eq. (8), this gives the correct relationships between the forces at the nodes.

$$\begin{aligned} F_1 &= F_A + F_B \quad \text{and} \quad F_2 = F_B - F_A && (13)\\ 2F_A &= F_1 - F_2 \quad \text{and} \quad 2F_B = F_1 + F_2 && (14) \end{aligned}$$

Comparing Eq. (10) and Eq. (13) leads to $F_B = 0$, and gives $F_A = F_1$. Thus, the constraints between v_1, v_2, v_A and v_B in Eq. (6) and Eq. (7) provide the correct constraints. The multi-point constraints for the numerical analysis are implemented into the finite element analysis as follows:

$$2v_1 - v_A - v_B = 0 \quad \text{and} \quad 2v_2 + v_A - v_B = 0 \tag{15}$$

In summary, F_A is the applied force to the beam from which the moment $M = F_A s = F_1 s$ can be calculated for each increment. J_R is computed from Eq. (1) using the calculated moment. The displacement v_A is the loading parameter, which is increased during the simulations.

4.2 Bridging law adjustment for numerical modelling

The bridging law as derived in Eq. (5) has a singularity in $\delta = 0 : \sigma \to \infty$ (see Eq. 5). A micromechanical model [5] predicts that crack initiation starts at a finite stress value at the interface, which is reached as the deformation starts to take place. At this point, the opening at the interface will still be zero! The experimental bridging law needs to be adjusted to account for this finite stress level. Figure 5(a) shows one possible adjustment with an initial linear bridging law up to a crack opening of δ_1, followed by a nonlinear stress decrease (softening). As a second option, the bridging law in Figure 5(b) with a finite stress level at zero opening can be applied. It should be noted that in most numerical evaluations in the literature bridging laws are proposed according to method (a). However, it needs to be considered that in this case the initial increase introduces an artificial flexibility into the numerical model, which might lead to incorrect structural behaviour if cohesive elements are introduced throughout the model at a large number of possible fracture locations.

The energy uptake of the experimental bridging law is determined by calculating the area W_{exp} under the curve. Differentiation of Eq. (4), which leads to Eq. (5), results in a loss of the initial starting value J_0 (see Table 1). To ensure the same energy uptake during the simulated fracture process, it was decided to add this initial starting value J_0 into the adjusted bridging law:

$$\sigma_{\text{exp}} = \frac{\Delta J_{\text{ss}}}{2\delta_0}\left(\frac{\delta_0}{\delta}\right)^{\frac{1}{2}} \tag{16}$$

$$W_{\text{exp}} = \Delta J_{\text{ss}}\left(\frac{\delta_1}{\delta_0}\right)^{\frac{1}{2}} + J_0 \quad \text{for} \quad \delta \in [0, \delta_1] \tag{17}$$

$$W_{\text{exp}} = \Delta J_{\text{ss}} + J_0 \quad \text{for} \quad \delta \in [0, \delta_0] \tag{18}$$

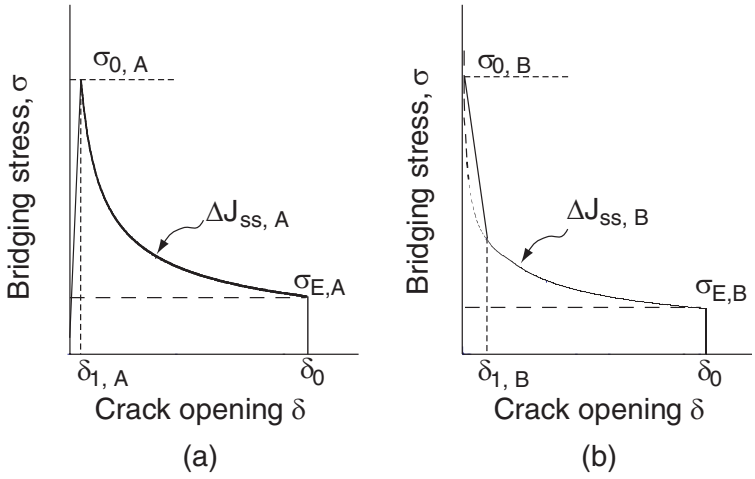

Figure 5. Comparison of different adjustments of the experimental bridging law

For bridging laws of method (a), the energy uptake of the adjusted bridging law is as follows:

$$\sigma(\delta) = \begin{cases} \frac{\Delta J_{\text{ss,A}}}{2\sqrt{\delta_0 \delta_{1,A}}} \left(\frac{\delta}{\delta_{1,A}}\right) & \text{for} \quad 0 < \delta < \delta_{1,A} \\ \frac{\Delta J_{\text{ss,A}}}{2\delta_0} \left(\frac{\delta_0}{\delta}\right)^{\frac{1}{2}} & \text{for} \quad \delta_{1,A} < \delta < \delta_0 \end{cases} \tag{19}$$

$$W_A = \Delta J_{\text{ss,A}} \left(1 - \frac{3}{4}\left(\frac{\delta_{1,A}}{\delta_0}\right)^{\frac{1}{2}}\right) \tag{20}$$

The parameter $\Delta J_{\text{ss,A}}$ in Eq. (20) is adjusted accordingly to the value of the chosen $\delta_{1,A}$ to achieve the same energy uptake as in Eq. (18):

$$\Delta J_{\text{ss,A}} = \frac{\Delta J_{\text{ss}} + J_0}{1 - \frac{3}{4}\left(\frac{\delta_{1,A}}{\delta_0}\right)^{\frac{1}{2}}} \tag{21}$$

Table 2 shows typical numerical values derived from the experimental results in Table 1 for the sizing A/ epoxy composite adjusted to method (a). It should be noted that for the symmetric half model all input values need to be divided by a factor 2. The maximum stress, $\sigma_{0,A}$, will then remain the same. The increase in the value for $\Delta J_{\text{ss,A}}$ will furthermore lead to a slight increase in the final bridging stress, $\sigma_{\text{E,A}}$, before separation (see Figure 5).

Table 2. Adjustment of the bridging law parameters for sizing A/epoxy (method (a))

J_0 [J/m^2]	ΔJ_{ss} [J/m^2]	$\delta_{1,A}$ [mm]	$\Delta J_{\text{ss,A}}$ [J/m^2]	$\sigma_{0,A}$ [MPa]
300	4000	0.001	4373	48.9
300	4000	0.005	4468	34.8
300	4000	0.05	4879	22.3

For the finite stress adjustment (method (b)), the maximum stress $\sigma_{0,B}$ is found by requiring that the area W_1 of the linear softening law in the range $0 \leq \delta \leq \delta_{1,B}$ must equal the area W_{exp} of the general bridging law in this range (see Eq. (17)). Area W_B is

given by

$$W_B = \frac{\Delta J_{\text{ss}}}{2}\left(\frac{\delta_{1,B}}{\delta_0}\right)^{\frac{1}{2}} + \frac{1}{2}\sigma_{0,B}\delta_{1,B} \tag{22}$$

Setting $W_{\text{exp}} = W_B$, while including the starting value J_0 as before, the maximum stress for a given $\delta_{1,B}$ is

$$\sigma_{0,B} = \frac{2J_0 + \frac{3}{2}\Delta J_{\text{ss}}\left(\frac{\delta_{1,B}}{\delta_0}\right)^{\frac{1}{2}}}{\delta_{1,B}} \tag{23}$$

Table 3 shows the typical numerical values derived from the experimental results in Table 1 for method (b). For the symmetric model, these input values again have to be divided by a factor of 2, while $\sigma_{0,B}$ remains identical. In comparison with method (a), the stress level $\sigma_{0,B}$ becomes significantly higher than $\sigma_{0,A}$ for the same δ_1 value. This is expected as J_0 is included within the range of $0 < \delta < \delta_{1,B}$ only.

Table 3. Resulting finite stress value (method (b)) for sizing A/epoxy

J_0 [J/m^2]	ΔJ_{ss} [J/m^2]	$\delta_{1,B}$ [mm]	$\sigma_{0,B}$ [MPa]
300	4000	0.005	180.0
300	4000	0.05	30.97
300	4000	0.5	7.2

Figure 6 shows the resulting analytical energy uptake for the adjusted bridging laws. The shape at the beginning of the crack bridging development depends on the choice of adjustment method and the value of $\delta_{1,A/B}$. All curves initially start at zero due to the integration, and not at a finite value of J_0 as proposed in the original curve fitting (see Table 1). It should be noted that in adjustment method (b), the curves become identical with the originally fitted curve (according to Eq. (4)), once $\delta_{1,B}$ is reached. All bridging laws result in identical energy uptake at the maximum crack opening due to the adjustments.

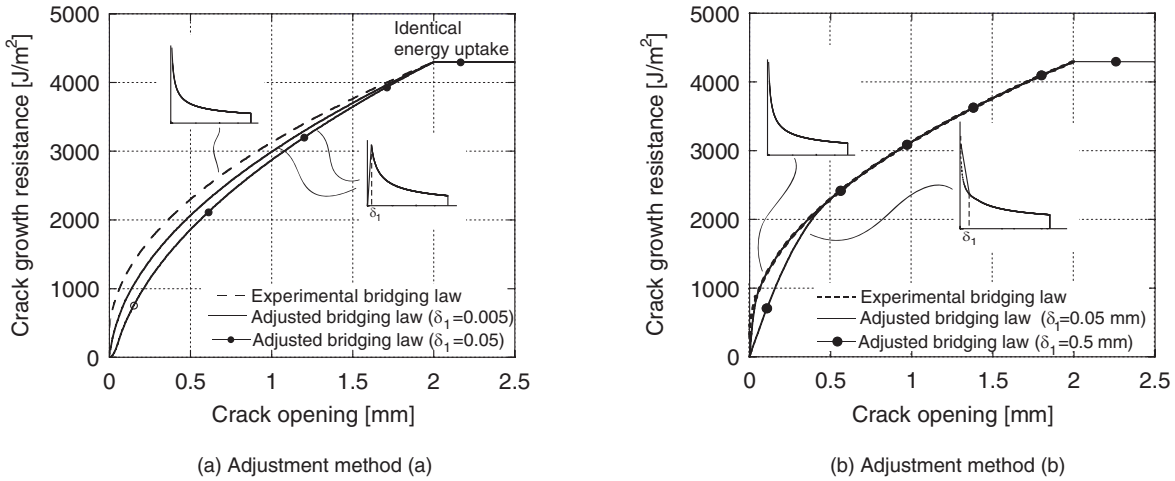

Figure 6. Comparison of analytical energy uptake form for different bridging law adjustments

4.3 Developed user subroutine uinter

Contact interaction, by default, describes the opposite behaviour of the bridging problem. For contanct, in general, there will be no stresses while both surfaces are apart from each other, while stresses will build up once surfaces interact. For a cohesive law, on the other hand, we wish for defined stresses while surfaces are apart at a specified distance. The contact option, however, is very versatile if the user subroutine uinter is programmed. Figure 7 shows the ABAQUS definitions to be used during implementation.

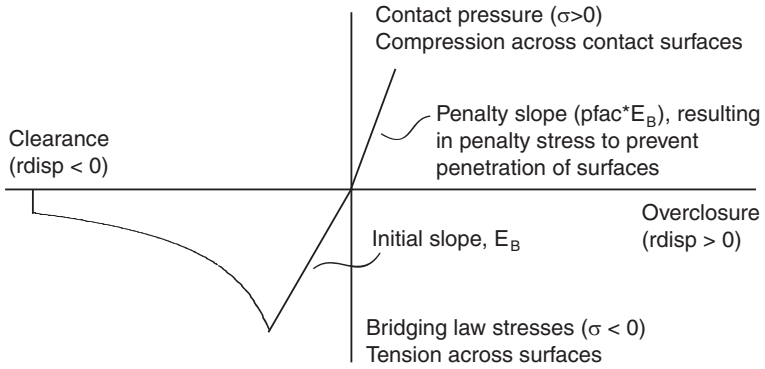

(a) Implementation of method (a)

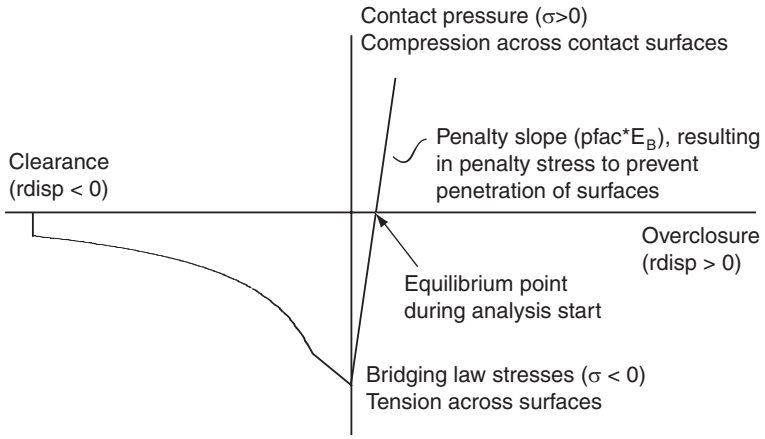

(b) Implementation of method (b)

Figure 7. Definition of signs in contact routine uinter

The routine needs to return the stresses at a given nodal displacement $rdisp$ and the tangent $\frac{\partial \sigma}{\partial \delta}$, which is the derivative of the stress with respect to the contact opening. As the slope of the curve is not a continuous function (as seen in Figure 7) a check for the value of $rdisp$ needs to be undertaken with every call of the user subroutine. It can furthermore be seen that the relative displacement of the node pair is given negative within ABAQUS if the two nodes are not overlapping, i.e. in the area where the cohesive law applies. Calculated stresses within the routine also have to be returned as negative. During overclosure, on the other hand, a penalty function needs to be applied to avoid deformation of the DCB specimen into itself. These stresses are returned as positive. Figure 7 (b) furthermore visualises the potential problem of adjustment method (b): the equilibrium point for the unstressed start condition is now moved into the region of overclosure. Ideally, an

infinitely steep stress increase to zero is wished for with an infinitely high penalty slope; however, as the opening-stress relationship needs to be uniquely defined for numerical reasons, overclosure is achieved.

The routine takes five input parameters in the following order:
$\Delta J_{\mathrm{ss,B}}, \delta_0, \delta_1$, pfac, method
A penalty factor $pfac$, provided as input, is used to calculate the penalty stresses. Typical values used for the penalty factor are between 10 - 10000. The parameter ”method” determines the use of adjustment method: ”1” for method (a), and ”2” for method (b).

5 Running the analysis

Figure 8 shows the stress component σ_1 on the deformed plot to help visualising the continuous deformation and fracture process during the numerical analysis (deformations not to scale). The bridging law data was applied as given in Table 2 with $\delta_{1,A}$=0.001 mm. Around the front section of the beam, the stress field is non-uniform due to the point-application of the bending forces. However, it can easily be seen that a uniform stress field under bending is established around the fracture zone. The displacement-controlled moment application as introduced in Section 4 with the distance k as given in Figure 3 is therefore validated.

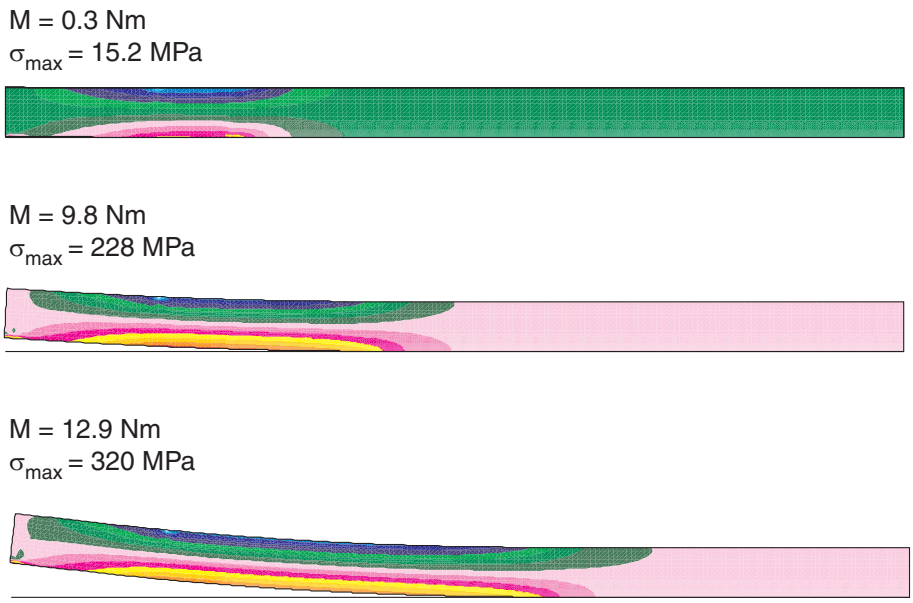

Figure 8. Beam deformation during crack advancement

A numerical analysis including softening material laws can become numerically unstable or non-converging during the run. Adjustments to the standard solver iterations might be required to optimise the analysis. The modified Riks method, which is an arc-length method, can be used to obtain solutions in the case of snap-back or decreasing force. The latter was encountered in the steady-state region of the analysis. The following points summarise the numerical differences between the two methods and outline ways to ”convince” ABAQUS to complete the analysis.

Oscillations could be present in the 8-noded elements in the contact zone during fracture progression, and midnodes were sometimes found to re-close near the crack tip, which was also reported in the literature [10]. In the case of a converged increment with

a re-closed midnode, elastic unloading could occur in the next increment when using the modified Riks method. As the re-closed increment solution was physically not valid due to a continuously progressing crack zone, the solution needed to be ignored and restarted with a smaller increment size. A restart method was implemented to check for invalid contact point closure in the uinter subroutine.

Method (a)
The analysis for method (a) was run displacement-controlled (see Section 4.1). No problems were encountered with method (a) for the given range of parameters (see Table 2) and the largest value of $\delta_{1,A}$=0.05 mm. With decreasing values for $\delta_{1,A}$, the mesh needed to be refined to achieve converging crack progression during the analysis. This is due to the steeper initial increase and decrease in the bridging law (increase in $\sigma_{0,A}$) while reducing $\delta_{1,A}$. Consequently, the material softening zone in the analysis is captured by a smaller number of elements. The critical point of the analysis is the passing of the opening value $\delta_{1,A}$ for the first contact point. Non-converging analyses (due to insufficient mesh refinement) will not converge once this point is reached. In that case, ABAQUS will reduce the increment size due to convergence problems until the analysis stops. It has been reported [10] that 2-3 elements should be present in the progress zone of the crack, i.e. the region where decreasing stresses due to the bridging law are encountered, to enable numerical stability. The smallest value of $\delta_{1,A}$ for currently successful numerical runs was 0.001 mm, which is equivalent to 1/2000 of the steady-state crack opening value δ_0. The required element length in the contact zone was less than 0.09 mm, leading to 1200 elements along the contact surface. Further mesh refinement to reduce $\delta_{1,A}$ was not undertaken.

Method (b)
Contrary to method (a), the analysis has sometimes problems right at the beginning of the first increment. This was attributed to the high stress value for $\sigma_{0,B}$ (see Table 3) and the fact that the contact elements tried to overlap with the master surface away from the crack tip to achieve equilibrium with zero stresses (see Figure 7(b)), rather than a certain number of elements within the softening zone. In this context the applied boundary conditions for the model proved to be very important, as the simulation tries to reach zero stress equilibrium along the contact surface at the beginning of the analysis. Consequently, the corner node at the end of the beam (on the contact surface) was not to be restricted in x and y-direction (see Figure 4). 1200 elements along the contact line were required to achieve convergence for $\delta_{1,B}$=0.05 mm. Analysis with smaller values of $\delta_{1,B}$ were not run successfully.

6 Comparison of numerical results

6.1 Numerical behaviour method (a)

Figures 9 show that the influence of mesh refinement is negligible for the crack opening versus crack growth resistance curve. As expected, the full model furthermore shows the same results as the symmetric half model, thereby validating the contact approach with a Master curve/ surface as symmetry line as introduced in Figure 3. Figure 9(c) and (d) show that the influence of $\delta_{1,A}$ on the crack growth resistance is relatively small for values of $\delta_{1,A} \leq 0.005$ mm as expected from the analytical investigation.

The initial increase up to $\delta_{1,A}$ in the $\sigma - \delta$ plot in Figure 5(a) can be considered a numerical necessity. Numerical trials have shown that analyses run smoother with this

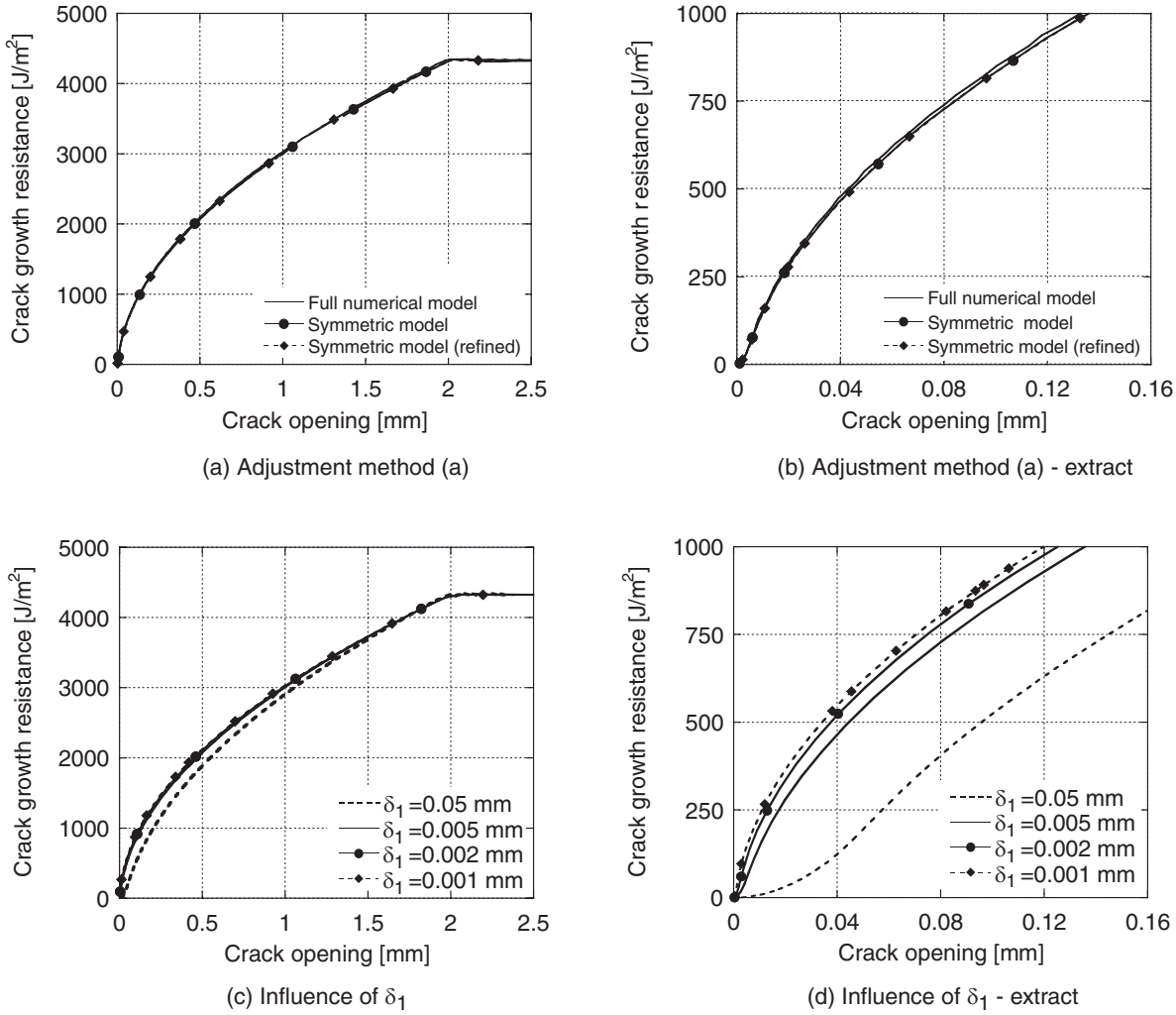

Figure 9. (a) and (b): Model and mesh refinement studies with $\delta_{1,A}$=0.005 mm; (c) and (d): Influence of $\delta_{1,A}$

option (compared to the finite stress value in method (b)) as long as $\delta_{1,A}$ is not chosen too small. However, this "artificial" stiffness of the cohesive law adds additional false flexibility to the structure. The influence of this false flexibility can be investigated by visualising the crack opening ($\delta = 2u_{2,\text{interface}}$) in comparison to the material deformation ($u_{2,\text{mat}} = u_{2,\text{neutral axis}} - u_{2,\text{interface}}$) at the neutral axis positioned above the crack notch. This is the same position as used for the measurement of the experimental crack opening. The material deformation therefore visualises whether the material expands or contracts due to the applied moment and the effect of the bridging stresses. Without a bridging effect, contraction of the beam material is expected during free bending deformation due to the Poisson effect. However, as seen in Figure 10, by including the bridging law, the material is initially forced to expand in the normal direction while stresses act on the interface. During the stage of initial loading prior to reaching $\delta_{1,A}$, the material deformation is linear and positive. Within the softening regime ($\delta_{1,A} < \delta < \delta_c$), the expansion reduces in a non-linear fashion as expected due to the bridging shape of the softening regime and becomes negative. To keep the influence of the artificial flexibility small, the interface stiffness should be higher than the stiffness of the composite material itself. As it is not possible to compare stiffnesses directly from the cohesive law due to the displacement-stress relationship, the influence of the parameter $\delta_{1,A}$ becomes clear by comparing the material deformation for different values of $\delta_{1,A}$ with the crack open-

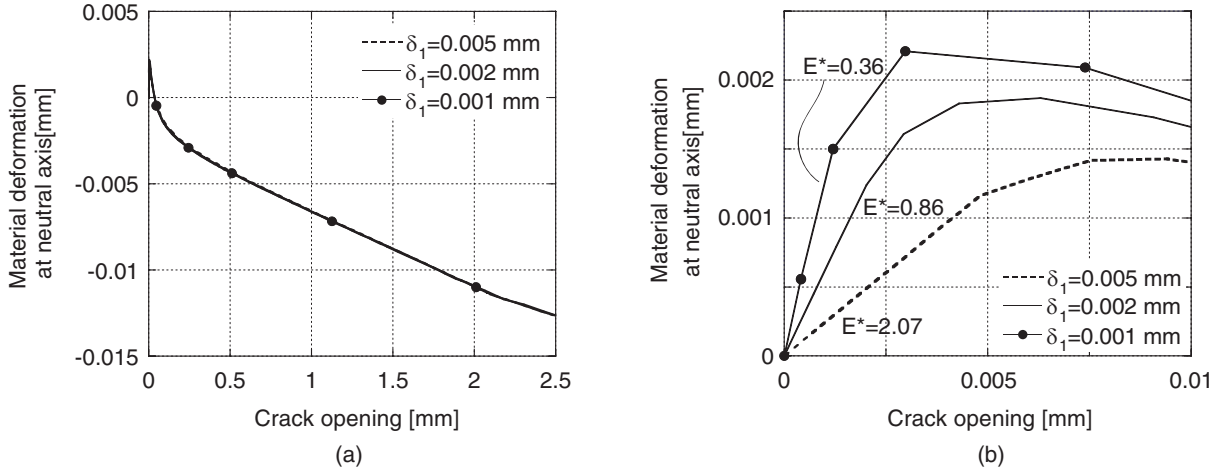

Figure 10. Structural deformations due to artificial flexibility

ing at the interface. Figure 10(b) demonstrates the local influence on the deformation of the model. The stiffness E* shows the ratio between the interface deformation and the material deformation at the neutral axis (E*= $\frac{u_{\text{interface}}}{u_{\text{mat}}}$) during the initial stress increase of the bridging law. It is unfortunately not possible to extract a limit value for $\delta_{1,A}$ from this plot, as the values obviously depend on an internal length scale (4 mm, the distance to the neutral axis, in this case). It is felt that the interface deformation should be smaller than the deformation of the material at the neutral axis ($E^* \ll 1$), so as a result, $\delta_{1,A}$ should be kept at its minimum value of 0.001 mm.

6.2 Numerical behaviour of method (b)

Table 3 demonstrated that the finite stress value increases rapidly with a decreasing value of $\delta_{1,B}$. This in turn leads to numerical problems, as elements start to turn inside out at the start of the analysis (see Section 5). The value of $\delta_{1,B}$=0.05 mm was found to lead to converging results for an element size of 0.09 mm, and as the cohesive law starts to follow the original curve exactly at $\delta_{1,B}$, this value is considered small enough to accurately describe the on-going deformations. In the following results, the value is not varied.

Figure 11 demonstrates that the influence of mesh refinement for method (b) is negligible for the crack opening versus crack growth resistance curve.

Figure 12 compares the initial deformation of the interface prior to crack development for both methods. It can be seen that mesh refinement for method (b) also does not alter the displacement results significantly. In comparison to the results from method (a), the crack opening at the interface now remains zero up to a material deformation of 0.002 mm at the neutral axis. This was to be expected with a finite stress value at zero opening. However, the initiation value of 0.002 mm depends on the choice of the finite stress level for method (b) and therefore $\delta_{1,B}$. There is no further validation of this statement due to the numerical problems associated with reducing $\delta_{1,B}$.

6.3 Crack length vs. crack growth resistance

Figure 13 shows the difference in crack length prediction for the two methods of cohesive law. The crack tip position for each numerical increment was determined based on a critical crack tip opening. For method (a), the critical crack tip opening was set to $\delta_{1,A}$, as the first part of the cohesive law is only a numerical simplification, and crack initiation occurs once this first part is overcome. For method (b), a small tolerance of 1e-6 mm was

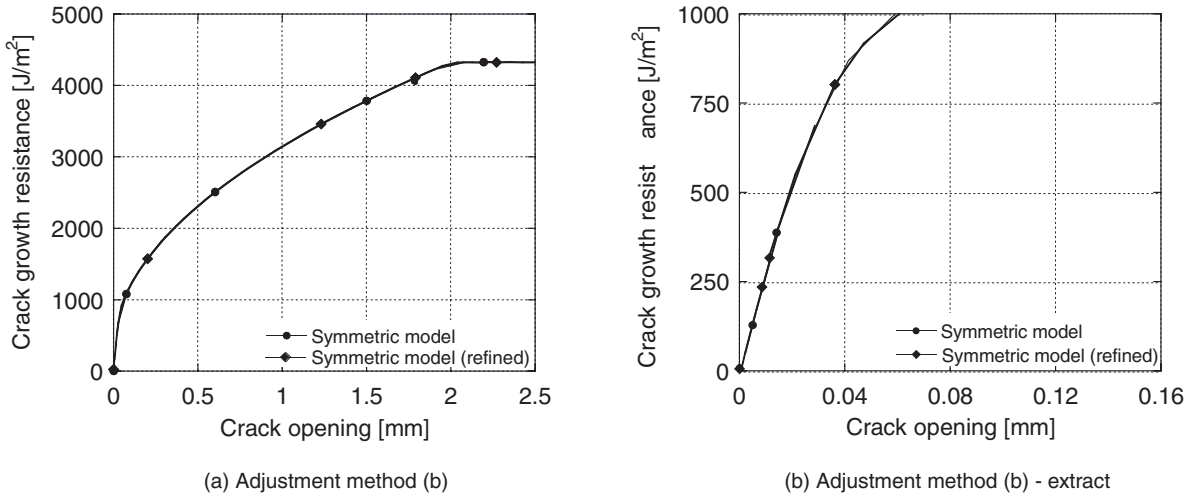

(a) Adjustment method (b)

(b) Adjustment method (b) - extract

Figure 11. Method (b) with $\delta_{1,B}$=0.05 mm

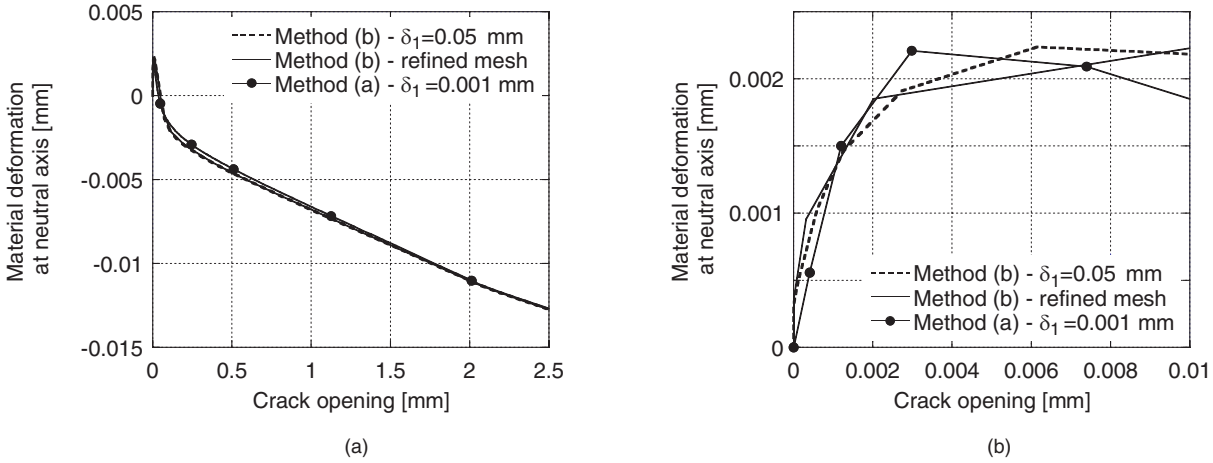

(a)

(b)

Figure 12. Influence of mesh refinement

assumed for the critical crack opening. However, the crack tip position is not sensitive to a reasonable range of tolerance values between 1e-6 mm and 1e-3 mm.

For the onset of steady state crack growth, very similar values for the crack length are predicted, as expected from the similar cohesive law shapes at this point. Method (a) shows some differences for the larger value of $\delta_{1,A}$ of 0.05 mm, which is due to the method of determining the crack tip position. For smaller values of $\delta_{1,A}$, good convergence is observed. At the start of crack growth, method (b) predicts a smaller crack growth for the same crack growth resistance, which is due to the incorporation of J_0 in the first part only. Due to the way of determining the onset of cracking for method (a), both methods now result in a finite value for the crack growth resistance at crack initiation of around 5-50 J/m^2. This value, is, however, much smaller than the measured values of J_0. Method (a) will reach the correct crack growth resistance only at the maximum crack opening (steady-state), while due to the incorporation of J_0 within the first part of the cohesive law, method (b) will reach the correct curve at $\delta_{1,B}$, which is small compared to the maximum crack opening. Method (b) is therefore giving more accurate results and is used in the following to derive the results for the different bridging laws.

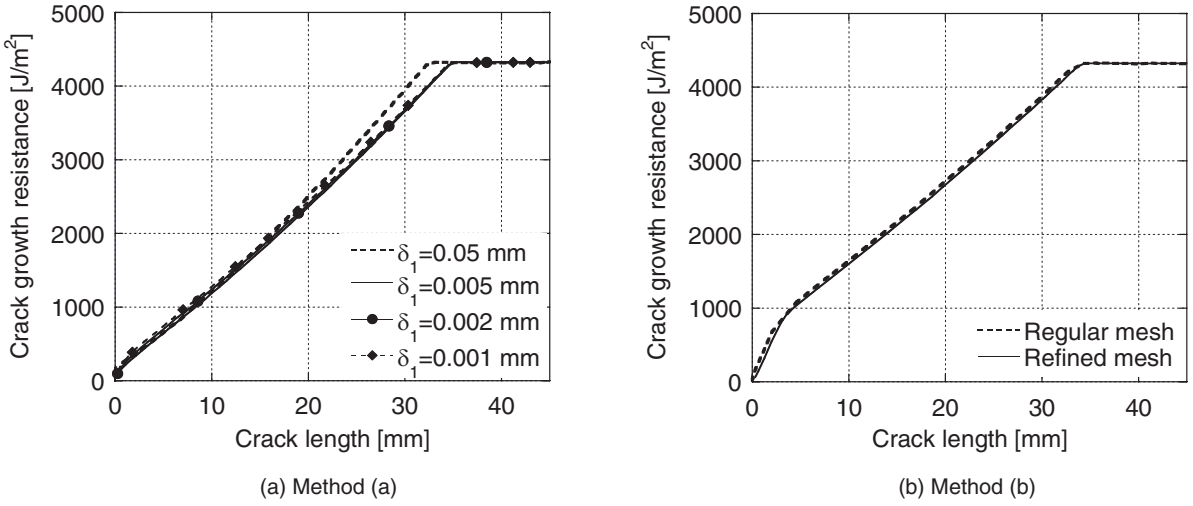

Figure 13. Predicted R-curve for tested specimen (H=8mm)

7 Comparison of results for different bridging laws

Figure 14 shows the resulting crack growth resistance predictions for two sets of data from Table 1 (sizing A/ epoxy and sizing A/ polyester) with one set of experimental data each, using numerical method (b) of bridging law approximation with a value of $\delta_{1,B}$=0.05 mm. The overall fit of the exemplary experimental curves is quite satisfactory. Discrepancies between the chosen curve fit in Eq. (5) and the experimental data are not due to numerical problems, but the curve fit itself. The curve fitting and detailed comparison with experimental data was discussed previously [3].

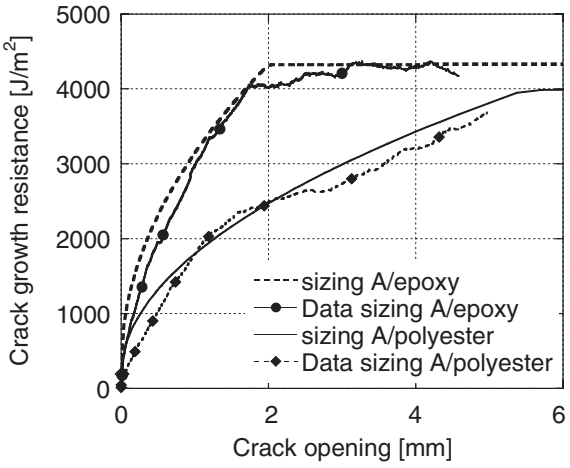

Figure 14. Comparison of numerical and experimental crack growth resistance

Figures 15 show the distinct differences in the R-curve and crack opening versus crack extension behaviour for the two composite systems. The crack extension is nearly linear with crack growth resistance due to the shape of the bridging law. The same observation

was made in previous work for carbon fibres using a different numerical approach [9]. It can furthermore be seen that the larger value of δ_0 in the bridging law for sizing A/ polyester (see Figure 2(b) and Table 1) leads to a significantly larger crack extension for a similar crack growth resistance. This was also observed experimentally.

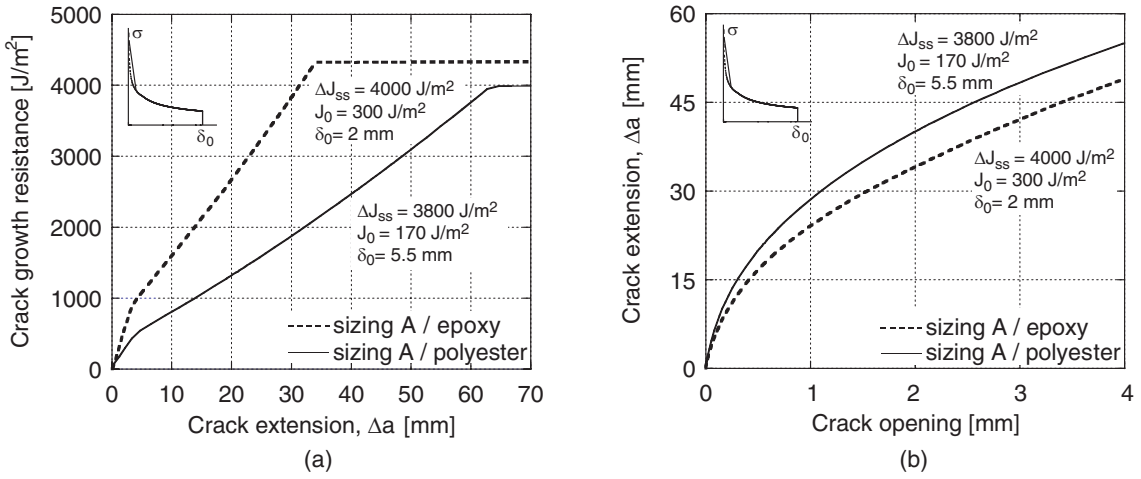

Figure 15. (a) Predicted R-curves as a function of crack extension and (b) crack opening vs. crack extension curve

The numerical model can furthermore be applied to study the detailed crack shape at specified loads or crack opening values. Figure 16(a) shows the crack opening for a specified crack growth resistance of J_R=3100 J/m^2. As also seen in Figure 14, the crack opening δ_0 is larger for a given crack growth resistance for sizing A/ polyester. The two corresponding unbridged profiles (same crack extension and applied moment) are also indicated in the figure. Of interest is the fact that the shape of the profile varies significantly in the crack tip vicinity. This difference is due to the continuously decreasing shape of the bridging law [11]. Figure 16(b) shows how the crack shapes vary for two crack opening values of δ_0=0.3 mm and δ_0=1.2 mm. For the same crack opening, the crack extension for the sizing A / polyester system will be higher, and the crack growth resistance J_R will be significantly lower.

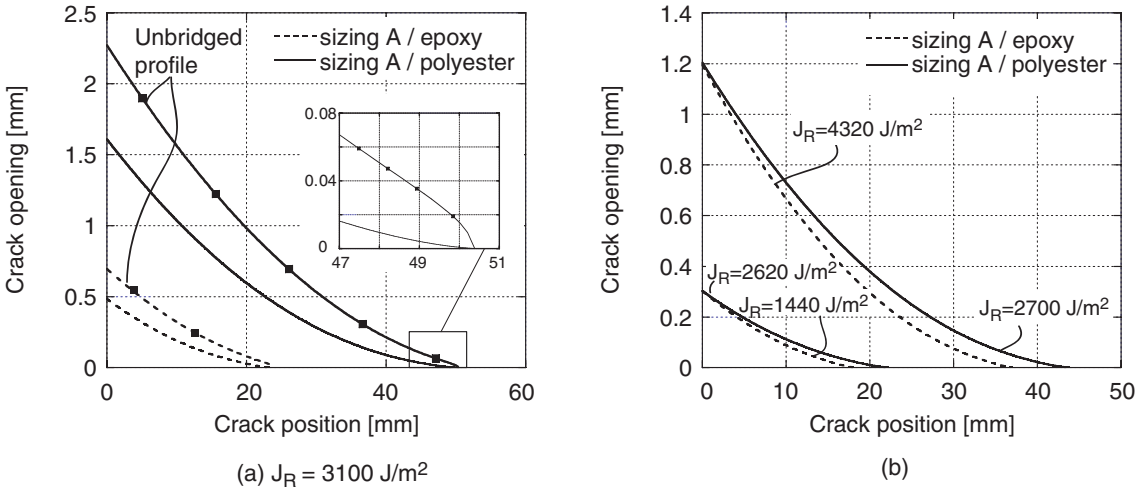

Figure 16. Comparison of crack opening shapes

References

[1] J.R. Rice. A path independent integral and the approximate analysis of strain concentration by notches and cracks. *Journal of Applied Mechanics*, 35:379–386, 1968.

[2] B.F. Sørensen and T.K. Jacobsen. Large scale bridging in composites: R-curves and bridging laws. *Composites: Part A*, 29A:1443–1451, 1998.

[3] S. Feih, J. Wei, P.K Kingshott, and B.F. Sørensen. The influence of fibre sizing on strength and fracture toughness of glass fibre reinforced composites. *Composites: Part A*, 2004. accepted.

[4] Z. Suo, G. Bao, and B. Fan. Delamination R-curve phenomena due to damage. *Journal of Mechanics and Physics in Solids*, 1(40):1–16, 1992.

[5] S.M. Spearing and A.G. Evans. The role of fibre bridging in the delamination resistance of fiber-reinforced composites. *Acta Metallica Materials*, 40(9):2191–2199, 1992.

[6] J.C.J. Schellekens and R. De Borst. On the numerical integration of interface elements. *International Journal for Numerical Methods in Engineering*, 36:43–66, 1993.

[7] C.G. Davila, P.P. Camanho, and M.F. de Moura. Mixed-mode decohesion elements for analyses of progressive delamination. In *42nd AIAA/ASME/ASCE/AHS/ASC Structures, Structural Dynamics and Materials Conference*, number AIAA-01-1486, 2001.

[8] J. Chen, M. Crisfield, A.J. Kinloch, E.P. Busso, F.L. Matthews, and Y. Qiu. Predicting progressive delamination of composite material specimens via interface elements. *Mechanics of composite materials and structures*, 6:301–317, 1999.

[9] T.K. Jacobsen and B.F. Sørensen. Mode I intra-laminar crack growth in composites - modelling of R-curves measured from bridging laws. *Composites: Part A*, 32:1–11, 2001.

[10] Y. Mi, M.A. Crisfield, and G.A.O. Davies. Progressive delamination using interface elements. *Journal of Composite Materials*, 32:1246–1272, 1998.

[11] J.E. Lindhagen, N. Jekabsons, and L.A. Berglund. Application of bridging-law concepts to short-fibre composites. 4. FEM analysis of notched tensile specimens. *Composites Science Technology*, 60:2895–2901, 2000.

Bibliographic Data Sheet **Risø–R–1463(EN)**

Title and author(s)

Modelling cohesive laws in finite element simulations via an adapted contact procedure in ABAQUS

Stefanie Feih

ISBN	ISSN
87–550–3321–0	0106–2840

Dept. or group	Date
AFM-KOM	July 2004

Groups own reg. number(s)	Project/contract No.
	1620043-00

Sponsorship

Pages	Tables	Illustrations	References
21	3	16	11

Abstract (Max. 2000 char.)

The influence of different fibre sizings on the strength and fracture toughness of composites was studied by investigating the characteristics of fibre cross-over bridging in DCB specimens loaded with pure bending moments. These tests result in bridging laws, which are obtained by simultaneous measurements of the crack growth resistance and the end opening of the notch. The advantage of this method is that these bridging laws represent material laws independent of the specimen geometry. However, the adaption of the experimentally determined shape to a numerically valid model shape is not straightforward, and most existing publications consider theoretical and therefore simpler softening shapes. Two possible methods of bridging law approximation are explained and compared in this report. The bridging laws were implemented in a numerical user subroutine in the finite element code ABAQUS. The main emphasis of this report is based on the numerical aspects of the different approaches, i.e. implementation, mesh sensitivity and numerical convergence.

Descriptors

Bridging laws; Glass fibre composites, numerical modelling, ABAQUS

Available on request from:
Information Service Department, Risø National Laboratory
(Afdelingen for Informationsservice, Forskningscenter Risø)
P.O. Box 49, DK–4000 Roskilde, Denmark
Phone (+45) 46 77 46 77, ext. 4004/4005 · Fax (+45) 46 77 40 13
E-mail: risoe@risoe.dk